Design of NbN based Kinetic Inductance Detectors for polarimetric plasma diagnostics

F. Mazzocchi[1], E.F.C. Driessen[2], S. Shu[2], M. Merker[3], K. Ilin[3], M. Siegel[3], A. Meier[1], D. Strauß[1] and T. Scherer[1]

[1]Karlsruhe Institute of Technology (KIT IAM-AWP), Eggenstein-Leopoldshafen, Germany
[2]Institut de Radio Astronomie Millimétrique (IRAM), Grenoble, France
[3]Karlsruhe Institute of Technology (KIT IMS), Karlsruhe, Germany

ABSTRACT

In this paper we present the design of a custom Kinetic Inductance Detector (KID) tailored for polarimetric diagnostics of magnetically confined fusion plasma. The detector is of the Lumped Elements (LEKID) kind and is based on a crossed 2x2 pixel design for polarization sensitivity. Simulations have been performed to tune device parameters like resonance frequency, cross-talking and coupling with the microstrip feed line, taking into consideration the requirements of the final instrument and the field of application. The devices have been designed for optimal absorption at 1.3 THz, the chosen probing frequency for the final instrument, and they resonate in a range from 0.8 to 1.1 GHz. The characterization of the thin Niobium Nitride (NbN) film and the first S_{21} parameter measurements performed on patterned thin films deposited on 330 µm High Resistivity Silicon (HRSi) substrates are also presented.

I. Introduction

In magnetically-confined nuclear fusion, polarimetry is a very well established diagnostic technology capable of measuring fundamental plasma parameters, such as poloidal field and plasma current density [1,2,3,4]. This technique aims at measuring the Faraday rotation angle induced in a linearly polarized laser beam travelling through a magnetized medium, such as a fusion plasma (fig. 1). In the non-relativistic limit, it is given by [5]:

$$\Delta\theta_F = \frac{e^3}{2\epsilon_0 m_e^2 c}\frac{1}{\omega^2}\int n_e(z)B_\parallel(z)dz$$

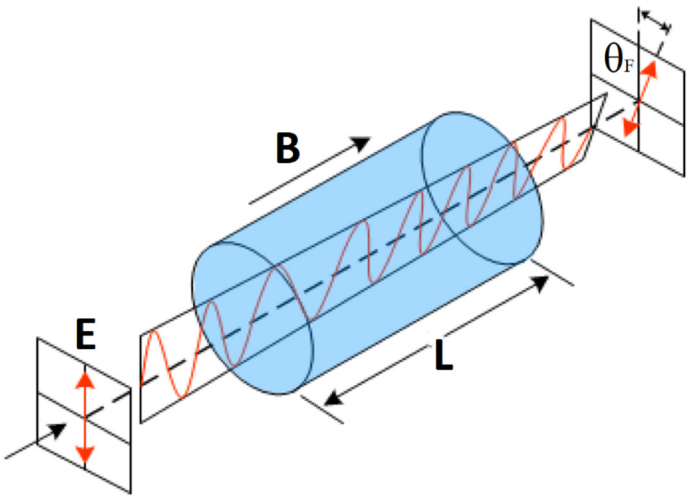

Figure 1 Schematic representation of Faraday effect

where $B_\parallel(z)$ is the component of the magnetic field parallel to the line of sight and n_e is the electron density. The current crop of polarimetric systems is designed around gas lasers emitting in the THz range that present several issues related to their price, stability, footprint and health hazard. Examples of such lasers are the HCN @ 337 µm [6,7,8], HCOOH @ 433 µm [9] and DCN @ 195 µm [10,11]. Electro-mechanical components part of some of the various configurations historically adopted [12] also represent a reliability weak point and their occurrence should be limited as much as possible. Additionally, hybrid interfero-polarimetric systems, like those installed on JET and LHD [11,13] suffer from the presence of vibrations and require active damping support systems. Given these premises, we opted to develop a pure polarimetric system with fewest moving parts as possible and inexpensive components in an effort to maximize availability and reduce inspection and maintenance down-time. Finally, we require the instrument to be able to characterize the poloidal plasma profile in its entirety. A multi-line-of-sight configuration with a dedicated polarimeter for each of the different optical axis crossing the plasma is therefore desirable. With these premises in mind, we decided to use a Kinetic Inductance Detector (KID) [14] as detector coupled to a frequency multiplier chain (FMC) cw source [15]. The probing frequency was chosen to be 1.3 THz, after considerations involving the typical conditions found in a modern tokamak and the system requirements [16].

Originally developed for astrophysical observations [17,18,19,20,21], KIDs can in principle be employed for plasma diagnostics applications. Their main advantages over other kind of detectors include a very simple, single layer structure that can be realized with conventional

photolithographic techniques, fast action and frequency division multiplexing (FDM) readout, where a single transmission line is able to read-out a large number of pixels simultaneously. Thanks to these characteristics, the final instrument can be realized with a very limited footprint, enabling the implementation of multiple line-of-sight configurations. KIDs can be also designed to be polarization sensitive, in which case only one detector is necessary and the mechanical polarization status modulator and selection stage can be both removed. This additionally simplifies the final instrument optical scheme and improves reliability. Following these guidelines, the Lumped Elements KID (LEKID) [22,23,24,25,26,27] was selected as development candidate, since it has the distinctive advantage of not requiring any antenna, unlike, for example, KIDs based on quarter-wave resonators [28,29]. The detector will be equipped with a backshort deposited on the backside of the chosen substrate acting as ground plane for the microstrips transmission lines lying above it. The presence of the backshort has the benefit of selecting a narrow detection bandwidth and increasing the absorbance of the incoming radiation within it, a particularly useful feature in an environment flooded with strong background radiation like the one coming from an ignited fusion plasma.

II. Theoretical Background

KIDs consist of superconducting resonant circuits characterized by their frequency $\omega_0 = 1/\sqrt{LC}$ and intrinsic quality factor $Q_0 = \omega_0/\Delta\omega$, where $\Delta\omega$ represents the half power bandwidth of the resonance dip. The quality factor is a measure of the ratio between the fraction of energy stored in the resonator and the one dissipated. If we couple our resonator to a read-out line, we can also define a coupling factor k as

$$\kappa = \frac{1 - |S_{21,min}|}{|S_{21,min}|}$$

where $S_{21,min}$ is the complex transmission scattering parameter taken at the minimum of the resonance. We can also define a transmission-line quality factor $Q_C = Q_0/k$ and a 'loaded' resonator quality factor

$$Q_L = (1/Q_0 + 1/Q_C)^{-1}$$

Q_0 can be estimated via BCS and Mattis-Bardeen theory and it is a function of the real and imaginary part of the complex conductivity [30]. A calculation of the Q_0 for a film of NbN at 4.2 K and T_c ~11 K resulted in values in the order of 10^4. The aim is to design the coupling quality factor within a range of similar values, given that the detector response is maximized for $Q_0 = Q_C$ [31]. If the resonator is superconducting, photons with energy higher than the superconducting gap impinging on it can break Cooper pairs back into electrons. This increased density of quasi-particles changes in turn the surface reactance of the superconductor. The kinetic inductance L_K derives from the manifestation of the inertial mass of charge carriers in high frequency electrical fields and is given by [26]

$$L_K = \frac{\sigma_2}{d(\sigma_1^2 + \sigma_2^2)\omega}$$

where σ_1 is the real part of the general circuit conductivity and σ_2 the imaginary one, d is the thickness of the absorber thin film and ω the angular frequency. This effect can be measured via the complex scattering parameter S_{21} as a change in the resonance frequency.

III. Detector Assessment

The characteristics of the device to be realized include a simplified optical scheme with respect to existing ones, a small footprint and high reliability, while keeping both costs and maintenance low. This translates in the following requirements for the KID in development:

- higher critical temperature (T_C = 10 – 16 K) as compared to aluminum (T_C = 1.2 K);
- polarization sensitivity;
- limited number of pixels (2x2) to limit potential cross-talking and ease the FDM read-out;
- lumped elements design.

The material of choice for the deposition on the wafers is NbN [32,33]. This material presents the transition to superconductivity at higher temperatures compared to aluminum [25], greatly reducing the complexity and cost of the cooling system required to operate the device. Although initially a dual detector configuration was planned [16], the possible mismatch (and subsequent calibration needs [10]) in sensitivity between the two detectors led us to choose a polarization-sensitive multi-pixel single-detector. The detector unit is composed of four LEKIDs (fig.3) sub-units, rotated 90 degrees with respect to each other. It measures 5x3.67 mm, including the contact pads. This arrangement provides polarization sensitiveness along the two different planes while keeping dimensions compact. Each subunit comprises a 1x1 mm^2 inductive part in the form of a meandered, continuous line that is common for all the pixels, and a tunable interdigital capacitor (IDC). We employed a simplified impedance model [30] to estimate the geometrical parameters of the structures to be deposited on the Si substrate in order to obtain a good optical coupling between radiation (Z_0 = 377 Ω) and detector. The effective impedance of the device is

$$Z_{Eff} = \frac{1}{\frac{1}{Z_{KID}} + \frac{1}{Z_{Sub}}},$$

where

$$Z_{KID} = \frac{\rho_{NbN} s}{d_{NbN} w}$$

is the characteristic impedance of the KID (taking a reactance equal to zero), ρ_{NbN} is the resistivity of NbN just above T_C, d_{NbN} is the thickness of the thin-film, s and w are the separation between the meandered lines and their width, respectively. For the substrate impedance we have:

$$Z_{Sub} = j\, Z_{Si} \tan(\beta l),$$

with Z_{Si} representing the silicon typical impedance, $\beta = 2\pi/\lambda_{Si}$ the effective wave number of the probe radiation (1.3 THz) in silicon and $l = 250$ µm the thickness of the substrate. This number is chosen to be an odd multiple of $\lambda_{Si}/4$ to maximize the absorption. With this model we obtained values for w, s and d_{NbN} of 40 µm, 10 µm and 15 nm, respectively. The resulting absorbance factor, calculated as

$$\alpha = 1 - \left|\frac{Z_0 - Z_{Eff}}{Z_0 + Z_{Eff}}\right|^2,$$

is 0.98 (fig. 2), with a substrate thickness tolerance within 5 µm resulting in a minimum absorbance factor of roughly 0.6, comparable to the values employed in a large array like NIKA2 [23]. The readout line is 200 µm wide to obtain an impedance of 50 Ω for good matching with the electronics of the data acquisition system. We estimate a maximum cross polarization signal detection in the order of 5%, given the ratio between the length of the inductor lines (1mm) and of their connecting segments (40 µm). Additionally, a simulation of the current density distribution performed on the pixels with the Sonnet EM Software suite [34] shows how the values of J in the IDC are non-uniform and lower than those found

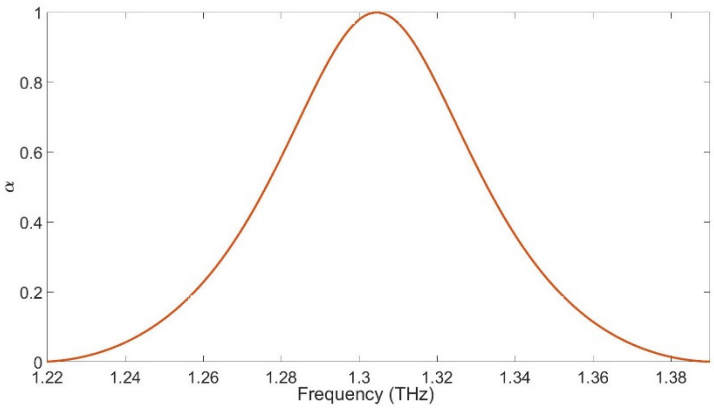

Figure 2 Calculated spectral response of KIDs for 250 µm HRSi substrate

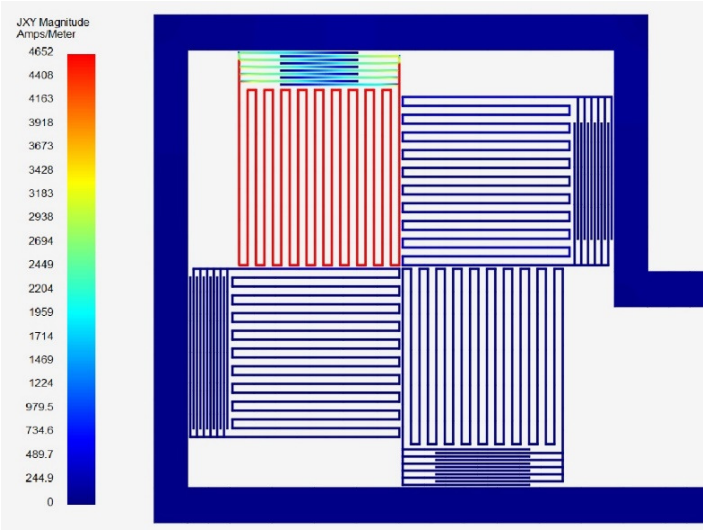

Figure 3 Pixel current density distribution analysis at one of the resonances. The IDC and inductor elements are clearly distinguished by the difference in value and homogeneity of the current density.

in the inductor (fig. 3), leading us to consider the capacitor contribution to the signal as negligible [35].

The coupling factor between the microstrip readout line and the LEKIDs influences the width and depth of the resonances, with wider and deeper dips corresponding to high coupling. Each sub-unit is designed to resonate at a different frequency, so that the signals can be extracted with a single readout line using frequency division multiplexing techniques. The resonances of the single sub-units were tuned by varying the number and length of the capacitor fingers (10 to 12 fingers, 700 to 900 µm). When properly designed, KIDs operate in a photon noise limited regime, where all the other possible noise sources don't give significant contribution to the total value. In this case, the noise level depends on the number of photons absorbed by the detector in a given bandwidth. It can be roughly estimated by [36]

$$NEP_{photon} \approx \sqrt{2h\nu \mathrm{P}}$$

where P is the power impinging on the detector at ν = 1.3 THz. To estimate the power impinging on the detector after one single roundtrip through the plasma, we adopted an absorption model based on the work of Yuan et al. [37]. At the typical conditions found in fusion reactors (with electron densities between 10^{19} and 10^{20} m^{-3}, cyclotron frequency of 140 GHz, electronic collisionality of 10 GHz and electronic temperatures around 10 keV), the absorption factor is comprised roughly between 0.05 and 0.4 (fig.4).

If we consider a source operating at 1.3 THz in continuous wave mode with a Gaussian beam profile, an

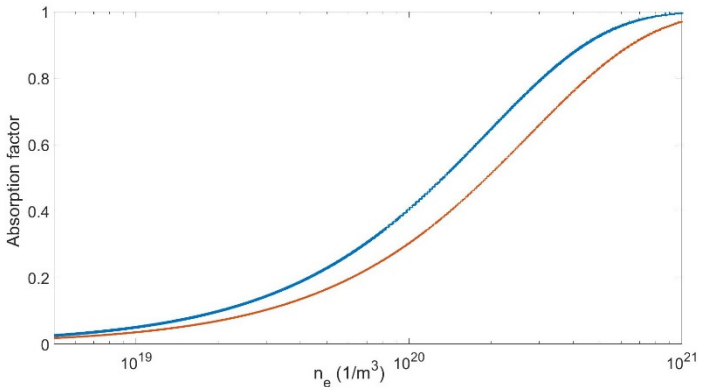

Figure 4 Calculated absorptivity vs plasma electron density for a DCN laser operating at 1.53 THz (blue curve) and 1.3 THz FCM source (orange curve).

output power of 0.1 mW and taking into consideration issues like beam divergence and losses from other optical elements along the beam path, we can estimate the power impinging on the detector in a range between 0.5 and 4 μW. This results in an estimated optical NEP between $2.9*10^{-14}$ and $8.5*10^{-14}$ W/Hz$^{1/2}$, dominating over the recombination/generation noise [31] and representing the physical lower limit for the noise level in our application. Since these power levels are quite high, there is the possibility to generate relatively large thermal gradients in the detectors. Would this be the case, we plan to employ a combination of reduced power from the source and attenuators at the cryostat window to reduce the incoming power to more manageable levels.

IV. Simulations

In order to establish and validate our design, simulations of several scenarios were performed. The first aspect addressed was the resonance frequency of the single pixels (fig.5). Having a good separation in frequency between adjacent pixels is of utmost importance, since it is necessary to avoid overlapping of the resonance curves in order to correctly apply frequency division multiplexing to the output signal. The frequency range goes from ~0.8 to ~1.1 GHz. After tuning the resonance frequencies, the next step involved studying the crosstalk in a system composed by two identical pixels with the same resonance frequency. We performed calculations at several interpixel distances (10-to-100 μm in steps of 10) and adding shielding structures in the form of a 10 μm NbN strip surrounding either three (open box configuration) or four (closed box configuration, fig.6) sides of the LEKIDs subunits, in addition to pixels without shielding. In case of the open box configuration, the unshielded side is the one facing the readout line. This analysis was performed to further investigate the possibility of implementing the shielding while keeping a good coupling between pixels and the transmission line. Cross talk modifies the resonances shape and position [25, 27, 38], introducing

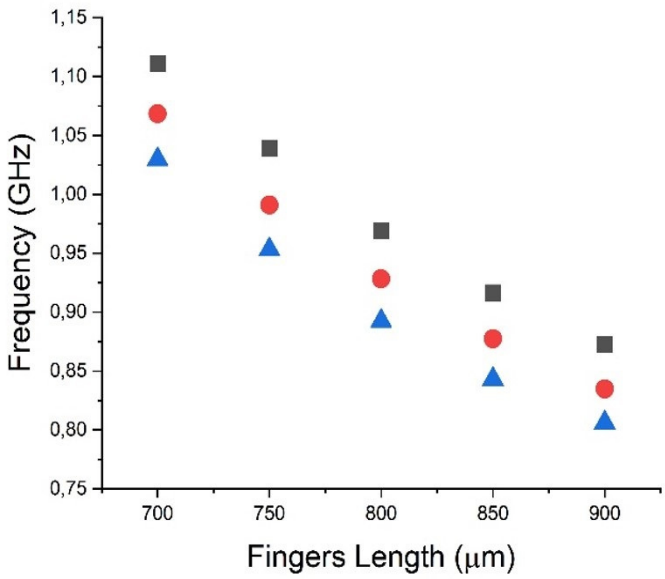

Figure 5 Simulated single pixel resonance frequency vs capacitor finger length, for 10 (black squares), 11 (red dots), 12 (blue triangles) fingers configurations.

parasitic coupling effects between pixels and parasitic resonance points (multiple dips). The further apart the two peaks, the stronger the cross-talk and, conversely, the spacing goes to zero in its absence. In the case of unshielded pixels, this phenomenon can be effectively mitigated by increasing the inter-pixel distance (fig.7, black squares) at the cost of considerably increased dimensions of the detector, but it cannot be eliminated completely. The shielding of the pixels, on the other hand, increases the separation between adjacent peaks, and the variation with respect to increasing the distance is much less pronounced than in the bare case. This result is in contrast to what can be found in ref. [23,24,25,26], where this kind of shielding is effectively employed to limit the cross-talk. We explain this difference as due to the polarization sensitive design we adopted, with the resonators tilted by 90 degrees with respect to each other. In our configuration, the cross coupling between pixels occurs between the long, continuous side of one of the inductors, and the much shorter segments at the bottom of its neighbour. When the shielding is present, the coupling is increased, since two long uninterrupted segments are facing each other, and the cross-talk is enhanced.

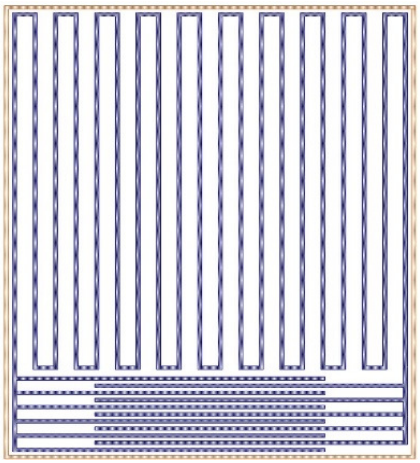

Fig. 6 Sonnet model of a single pixel complete with shield

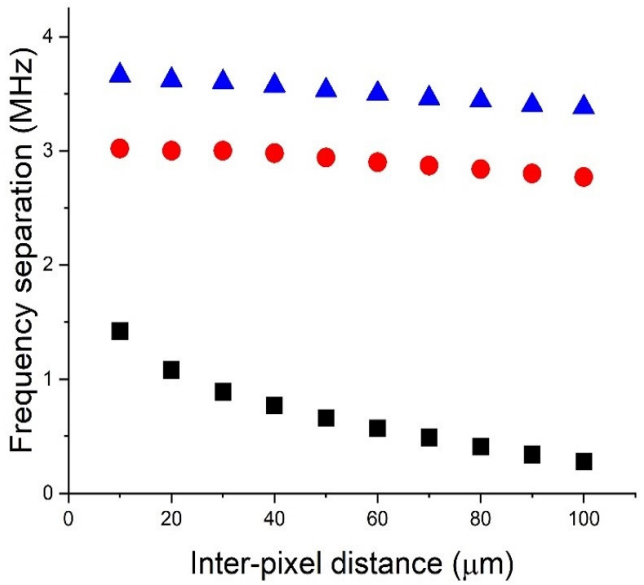

Figure 7 Simulated frequency separation of multiple resonance peaks vs interpixel distance in case of cross-talking with different shielding configurations (BOX – blue triangles, OPEN BOX – red dots, UNSHIELDED – black squares).

The third step of simulations addressed the study of the coupling between the KIDs and the readout line. The simulations were performed on a single-pixel system (11 capacitor fingers, 750 μm each), varying the distance from the readout line from 10 to 100 μm in steps of 10 μm. The values of Q_C are shown in fig. 8, from which it is apparent that the closed box configuration greatly limits the coupling, resulting in high Q_c values, between $5*10^4$–$1.9*10^5$. On the other hand, the bare and open box configuration fall inside the 10^4 range. The last step in the simulations aimed at the study of the prototypes, consisting in four different combinations of non-identical pixels. As it can be seen in fig. 9, there are no multiple peaks in the simulation results relative to the complete detector (black line), demonstrating that the resonance frequencies are separated enough to avoid this effect. There is no need, therefore, to increase the distance between the single resonators above 10 μm, resulting in a compact design. Fig. 9 also shows that there is a general shift of the resonance frequencies of the complete detector toward lower values compared to the simulated resonances of the single pixels (colored lines). This aspect can be justified by taking into consideration the modified geometry of the readout line and the additional coupling effects deriving from it. It can also be noted that this effect is stronger for the "faster" pixels, since their capacitance is lower and additional coupling effects have proportionally a larger impact.

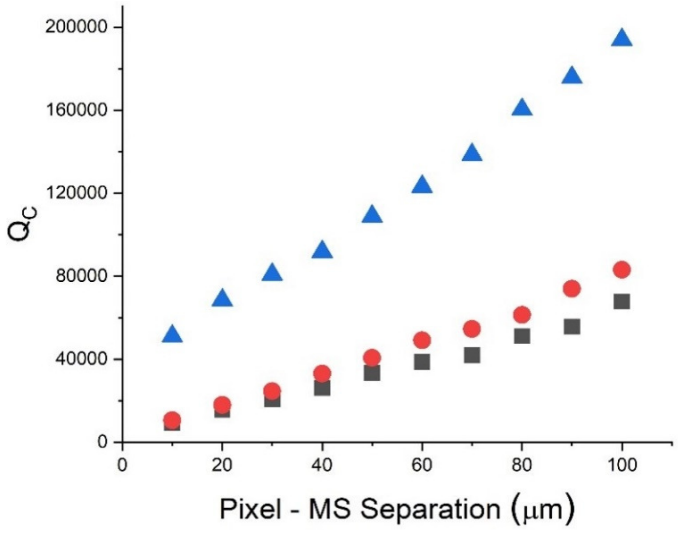

Figure 8 Simulated coupling quality factor of the pixels without shielding structures (black squares) and with closed (blue triangles) and open (red dots) configurations.

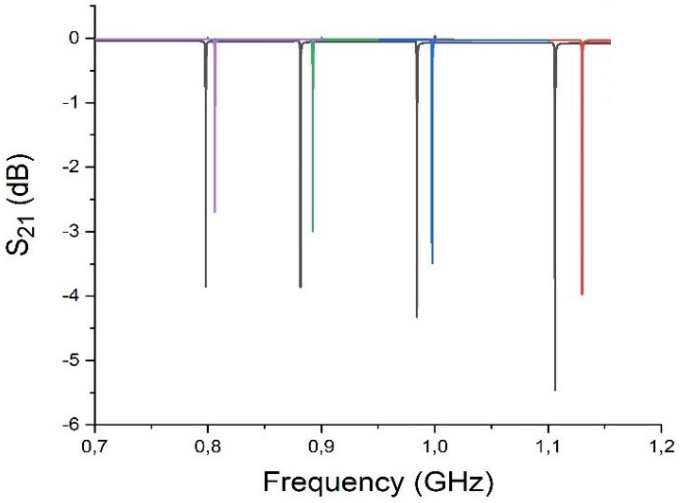

Figure 9 Simulation results of the Prototype 1 configuration (black curve) and of the single pixels (colored dips) composing the detector.

V. Characterization and First Measurements

The NbN film was deposited via a DC reactive magnetron sputtering process. For production reasons, this first batch of HRSi wafer was cut with a thickness of 330 μm. The backshort/ground plane is also composed by a NbN film, 400 nm thick in this case. The characterization of the NbN film was performed by measuring the R vs T and I vs V profiles of purposely designed test strips of 20 μm in width. The three test strips, one for each wafer, were bonded to a chip carrier installed on a dipstick. By slowly inserting the dipstick inside a helium dewar and letting it thermalize, we obtained the resistance profile as a function of temperature. I vs V data have been collected by fully submerging the test strips into helium, in order to obtain a stable temperature of 4.2 K. We then measured critical current densities of, respectively, $3.25*10^6$, $3.26*10^6$ and $3.31*10^6$ A/cm^2 for the three wafers. The R(T)-curves show critical temperatures around 11 K (fig. 10). The wafers don't show significant difference in performance, with normal state sheet resistivities in the order of 170 Ω/□ and transitions widths ΔT of approximately 0.5 K. The transition temperatures are in line with values found in

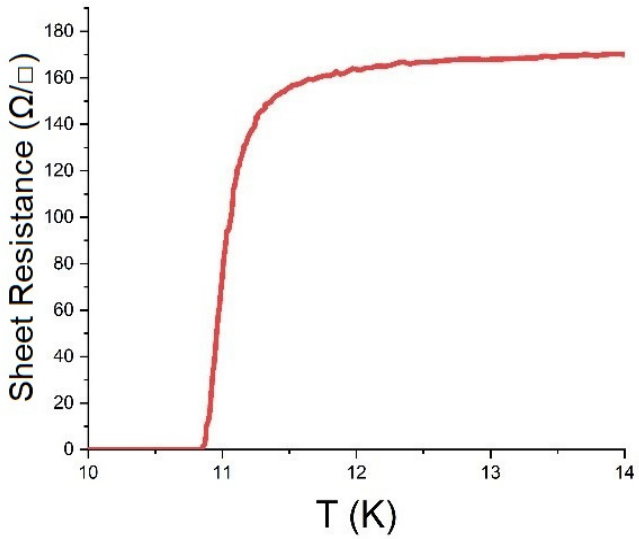

Figure 10 typical R/T profile of the superconducting test strips.

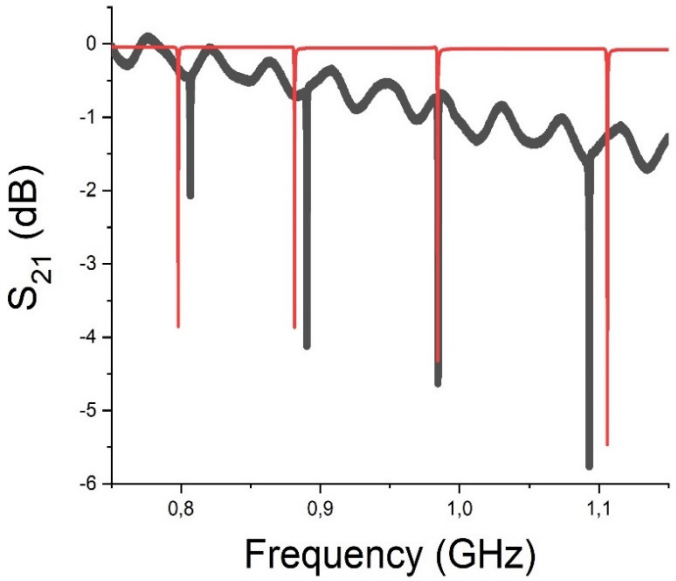

Figure 11 Measured (black curve) S_{21} parameter vs simulated (red curve). The measured curves have been offset with + 6dB for clarity purposes

literature for DC sputtered films of this thickness [27]. The measurements on the first prototypes have been performed by submerging the chips into liquid helium, similarly to what was done for the film characterization.

The resonators were excited and the response signal was obtained with a Vector Network Analyzer. We employed a 20 dB attenuator at port 1 of the VNA to limit the thermal noise injected in the system and to lower the risk of the exciting readout tone to saturate the resonator. The power of VNA was set to – 20 dBm, without any amplification at the read-out port. Taking into account the 20 dB attenuator effect, the original VNA signal still had a baseline of about -6dB that we decided to offset in the graph for clarity purposes. During the measurements we observed a typical temperature dependent behavior, where the resonances started to appear at the onset of superconductivity, and got deeper and shifted toward higher frequencies as we progressively inserted the dipstick inside the dewar. Fig. 11 illustrates the measurements performed on one of the prototypes, compared to the simulated curve obtained with Sonnet. On fig. 12 the peak number 3 from the very same measurement can be appreciated in more detail, together with the Lorentzian fit used to extract the values of the quality factors. This peak corresponds to the pixel used in the coupling tuning simulations. The resonance is very sharp and slightly asymmetrical but not very deep, standing at roughly -4 dB. The value for Q_C is approximatively $1.1*10^4$, quite close to the calculated one (Fig. 8, bottom left point) equal to $9.1*10^3$. We attribute the shallowness and low signal to a series of factors including losses: the Q_0 of the simulated peak has a value of around $3*10^6$ while the measured one is much lower at $6.4*10^3$. The relatively high temperature of the measurements must be taken into account since KIDs are typically operated at $T_C/10$ to reduce the presence of quasiparticles in the superconductor. The higher the temperature, the higher the contribution to the resonator losses given by the superconductor quasi particles population. Additionally, whereas the detectors were designed around a 250 µm substrate for optimal coupling with incoming radiation, the NbN thin films were deposited on a 330 µm thick substrate. The resulting impedance mismatch between the microstrip and the read-out electronics of the VNA determined the detected low-baseline signal.

The ripples in the baseline signal also suggest the presence of a standing wave oscillating along the transmission line, sign of the aforementioned mismatch at the detectors ports. Nevertheless, the simulations were able to correctly predict the resonance frequencies of the pixels.

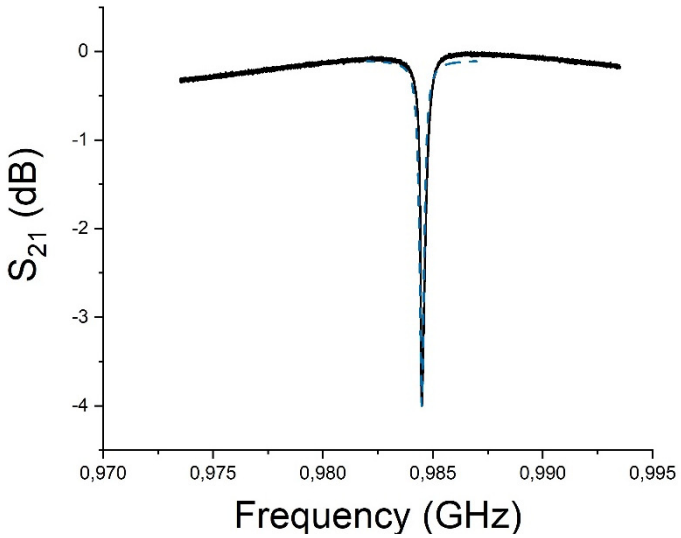

Figure 12 Prototype resonance number 3 as measured (black line) and relative fit (blue dashed line)

VI. Conclusions

In this work we presented the design process of Kinetic Inductance Detectors to be employed in a polarimeter to be used in future magnetic confinement fusion reactors. The detector consists in a 4-pixel array, arranged in a crossed configuration for polarization sensitivity. The material of choice is NbN on a HRSi substrate, with an NbN ground plane / backshort. Simulations were performed in order to obtain a good range of different resonance frequencies, to study the crosstalk effect and to optimize the coupling factor between readout line and detectors. The simulated values show that the design fulfils the requirements for a coupling quality factor around 10^4. The calculations on the prototypes also showed no sign of crosstalk, proof that the single pixels resonance frequency are sufficiently far apart to avoid this effect. The pixels can be therefore packed closely together for a smaller detector footprint. Characterization measurements of the deposited NbN film show how the three wafers produced so far operate with analogous performances, a confirmation of the consistency of the deposition process. Additionally, the first measurements of the S_{21} signal are reported, with the detected frequencies matching those predicted by the simulations. The values for the coupling quality factor Q_C extracted from the data are in good agreement with those calculated from the simulations, and in general we recorded a low power signal that we explain as related to impedance mismatch, losses and realatively high temperature of the measurements. These tests serve as proof-of-concept: the production of prototypes on low losses substrates and modified microstrip geometry will represent the next step toward the optimization of the device for the final application.

VII. References

[1] W Kunz and TFR Equipe. First measurement of poloidal-field-induced faraday rotation in a tokamak plasma. Nuclear Fusion, 18(12):1729, 1978.

[2] H Soltwisch. Current density measurements in tokamak devices. Plasma physics and controlled fusion, 34(12):1669, 1992.

[3] A Boboc, B. Bieg et al., A novel calibration method for the JET real-time far infrared polarimeter and integration of polarimetry-based line-integrated density measurements for machine protection of a fusion plant (invited), Review Of Scientific Instruments 86(7): 091301, 2015

[4] H R Koslowski and H Soltwisch, Electron density and q profile measurements with the far-IR interferometer – polarimeter on the TEXTOR tokamak, Fusion Engineering and Design 34-35 (3):143, 1997

[5] S Mancuso and S R Spangler. Faraday rotation and models for the plasma structure of the solar corona. The Astrophysical Journal, 539(1):480, 2000.

[6] P Belland, D Veron, and LB Whitbourn. Mode study, beam characteristics and output power of a cw 377µm HCN waveguide laser. Journal of Physics D: Applied Physics, (18):2113, 1975.

[7] M Kawamura, I Okabayashi, and T Fukuyama. A capacitively coupled RF-excited CW HCN laser. IEEE journal of quantum electronics, 21(11):1833–1837, 1985.

[8] J B Zhang, X C Wei, et al., Output power stability of an HCN laser using a stepping motor for the east interferometer system. Journal of Instrumentation, 10(11):C11004, 2015.

[9] Y G Li, Y Zhou, et al. First electron density fluctuation measurement via the HCOOH laser far-forward collective scattering on HL-2A tokamak. Journal of Instrumentation, 11(02):C02002, 2016.

[10] A Mlynek, L Casali, et al.,, Fringe jump analysis and implementation of polarimetry on the ASDEX Upgrade DCN interferometer. Review of Scientific Instruments, 85(11):11D408, 2014.

[11] G Braithwaite, N Gottardi, et al., Jet polari-interferometer. Review of scientific instruments, 60(9):2825–2834, 1989.

[12] R. Imazawa, Y Kawano, T Akiyama, et al. Polarization measurement techniques suitable for ITER poloidal polarimeter. In Proceedings of the 41st Plasma Physics Conference on Plasma Physics (EPS2014)(IOP, Berlin, Germany, 2014) P, volume 5, 2014.

[13] T Akiyama, S Tsuji-Iio, R Shimada, et al. Co2 laser polarimeter for electron density profile measurement on the large helical device. Review of Scientific Instruments, 74(5):2695{2703, 2003.

[14] P K Day, H G LeDuc et al., A Broadband Superconducting Detector Suitable For Use In Large Arrays, Nature Vol.425, October 2003

[15] https://vadiodes.com/en/frequency-multipliers/?id=176

[16] F. Mazzocchi, G. Grossetti, et al., THz multi line of sight polarimeter for fusion reactors. Fusion Engineering and Design, 130(5): 1-5, 2018.

[17] A Monfardini, L J Swenson et al., NIKA: A millimeter-wave kinetic inductance camera, A&A 521, A29 (2010)

[18] G Vardulakis, S Withington, et al. Superconducting kinetic inductance detectors for astrophysics. Measurement Science and Technology, 19(1):015509, 2007.

[19] A Monfardini, A. Benoit, et al. A dual-band millimeter-wave kinetic inductance camera for the IRAM 30 m telescope. The Astrophysical Journal Supplement Series, 194(2):24, 2011.

[20] J Zmuidzinas and P L Richards. Superconducting detectors and mixers for millimeter and submillimeter astrophysics. Proceedings of the IEEE, 92(10):1597–1616,2004.

[21] J Schlaerth, A Vayonakis, et al. A millimeter and submillimeter kinetic inductance detector camera. Journal of Low Temperature Physics, 151(3):684–689, 2008.

[22] S Doyle, P. Mauskopf et al., Lumped Element Kinetic Inductance Detectors, Journal of Low Temperature Physics, Vol 151, 2008

[23] S Shu, M Calvo et al., Optical Response of LEKID Arrays, IEEE Transactions on Terahertz Science and Technology, vol.8, no.6, Nov 2018.

[24] M Roesch, F. Mattiocco, et al, Modeling and Measuring the Optical Coupling of Lumped Element Kinetic Inductance Detectors at 120-180 GHz, IEEE Transactions On Antennas And Propagation, Vol.61 (4) April 2013\

[25] S Shu, M Calvo et al., Prototype High Angular Resolution LEKIDs for NIKA2, Journal of Low Temperature Physics vol 193, 2018

[26] M Roesch. Development of Lumped Element Kinetic Inductance Detectors for mm wave astronomy at the IRAM 30 m Telescope. PhD thesis, Karlsruhe Intitute Of Technology, 2013, ISBN 9783731501107.

[27] S Wuensch, C Groetsch et al, Optimized LEKID Structures with Low Crosstalk for Large Detector Arrays, IEEE Transactions on Applied Superconductivity, Vol. 25 (3), June 2015

[28] J Gao, The Physics of Superconducting Microwave Resonators, PhD thesis, Caltech 2008

[29] B A Mazin, Microwave Kinetic Inductance Detectors, PhD thesis, Caltech, 2004

[30] S Shu, Large format LEKID arrays for millimeter wave astronomy, PhD thesis, IRAM Grenoble, 2019

[31] J Zmuidzinas, Superconducting Microresonators: Physics and Applications, Annual Review of Condensed Matter Physics, 2012.3:169-214.

[32] Y M Shy, LE Toth, and R Somasundaram. Superconducting properties, electrical resistivities, and structure of NbN thin films. Journal of Applied Physics, 44(12):5539–5545, 1973.
[33] R Schneider, B Freitag et al, Structural and Superconducting Properties Of Ultrathin NbN films on silicon, Crystal Research and Technology, Vol 44 (10), 2009
[34] https://www.sonnetsoftware.com/
[35] S Doyle, Lumped Elements Kinetic Inductance Detectors, PhD thesis, Cardiff University, 2008
[36] D Flanigan, H. McCarrick et al., Photon noise from chaotic and coherent millimeter-wave sources measured with horn-coupled, aluminum lumped-element kinetic inductance detectors, Applied Physical Letters 108, 083504 (2016)
[37] C Yuan, Z. Zhou et al., Propagation properties of broadband terahertz pulses through a bounded magnetized thermal plasma, Nuclear Instruments And Methods in Physics Research B 269 (2011) 23/29
[38] A Adane, G. Coiffard et al., Study of the behavior of Cross-talk in Hilbert KID array using Sonnet software, 11th Internation Workshop On Low Temperature Electronics, 81-84, 2014